# Dynamic rupture and stress change in a normal faulting earthquake in the subducted Cocos plate

AUTHOR(S):

Mikumo, Takeshi; Santoyo, Miguel A.; Singh, Shri Krishna

CITATION:

Mikumo, Takeshi ...[et al]. Dynamic rupture and stress change in a normal faulting earthquake in the subducted Cocos plate. Geophysical Journal International 2000, 140(3): 611-620

ISSUE DATE:

2000-03

URL:

http://hdl.handle.net/2433/193408

*Geophys. J. Int.* (2000) **140,** 611–620

# Dynamic rupture and stress change in a normal faulting earthquake in the subducting Cocos plate

Takeshi Mikumo, Miguel A. Santoyo and Shri Krishna Singh

*Instituto de Geofisica, UNAM, Ciudad Universitaria,* Cp 04510, *Mexico DF, Mexico. E-mail: mikumo@ollin.igeofcu.unam.mx*

Accepted 1999 October 15. Received 1999 September 27; in original form 1999 March 24

## SUMMARY

A large nearly vertical, normal faulting earthquake ($M_w = 7.1$) took place in 1997 in the Cocos plate, just beneath the ruptured fault zone of the great 1985 Michoacan thrust event ($M_w = 8.1$). Dynamic rupture and resultant stress change during the 1997 earthquake have been investigated on the basis of near-source strong-motion records together with a 3-D dynamic model.

Dynamically consistent waveform inversion reveals a highly heterogeneous distribution of stress drop, including patch-like asperities and negative stress-drop zones. Zones of high stress drop are mainly confined to the deeper, southeastern section of the vertical fault, where the maximum dynamic stress drop reaches 280 bars (28 MPa). The dynamically generated source time function varies with location on the fault, and yields a short slip duration, which is caused by a short scalelength of stress-drop heterogeneities. The synthetic seismograms calculated from the dynamic model are generally consistent with the strong-motion velocity records in the frequency range lower than 0.5 Hz.

The pattern of stress-drop distribution appears, in some sense, to be consistent with that of coseismic changes in shear stress resulting from the 1985 thrust event. This consistency suggests that the stress transfer from the 1985 event to the subducting plate could be one of the possible mechanisms that increased the chance of the occurrence of the 1997 earthquake.

**Key words:** dynamics, inversion, normal faulting, rupture propagation, shear stress, synthetic waveforms.

## INTRODUCTION

The south Pacific coastal region of Mexico, where the Cocos plate subducts beneath the North American plate, is one of the world's most seismically active zones. Large thrust earthquakes with low dip angles and shallow depths frequently occur on the upper interface of the subducting plate. In addition to these, large intermediate-depth normal faulting earthquakes also take place in the subducting slab: for example, the 1858 Michoacan ($M_s = 7.5$) (Singh *et al.* 1996), 1931 Oaxaca ($M_s = 7.8$) (Singh *et al.* 1985), 1973 Orizaba ($M_s = 7.3$) (Singh & Wyss 1976), 1980 Huajuapan de Leon ($M_s = 7.6$) (Yamamoto *et al.* 1984), and 1994 Zihuatanejo ($M_s = 6.6$) (Cocco *et al.* 1997; Quintanar *et al.* 1999) earthquakes. Most intermediate-depth earthquakes take place in the unbending and subhorizontal portion of the subducting plate, while a few occur somewhat closer to the trench.

A large nearly vertical, normal faulting earthquake ($M_w = 7.1$) occurred in the Michoacan segment of the Mexican subduction zone on 1997 January 11, just beneath the extensive ruptured zone of the great Michoacan thrust earthquake ($M_w = 8.1$) of 1985 September 19 (Fig. 1). An inversion of teleseismic *P* and *SH* waves, based on a horizontally propagating line source model, favoured a nearly vertical faulting mechanism (dip = 87°, strike = 105°, and rake = −110°) (Fig. 1a), and a centroid focal depth of 35 km (Santoyo *et al.* 1999). Two other moment tensor inversions (M. Kikuchi, personal communication 1997; Monthly Listing of the USGS 1997) also gave a vertical plane as one of the two nodal planes. Although there are some minor differences in focal mechanism solutions, the 1997 earthquake appears to have a nearly vertical fault at mid-depth in the subducting Cocos plate (Fig. 1b). We may regard it as a normal faulting event in view of the geometry of the subducting plate and the sense of the down-thrown side.

The 1997 earthquake was preceded by the 1985 large thrust event that occurred just above it. From the close proximity of their locations and relatively short time interval of 12 years, a causal relationship between the two events is expected. One possible explanation may be stress transfer (i.e. coseismic stress increase) from the 1985 event to the zone of the 1997 vertical fault in the subducting slab and its possible postseismic increase (Mikumo *et al.* 1999). Another tectonic force to enhance this

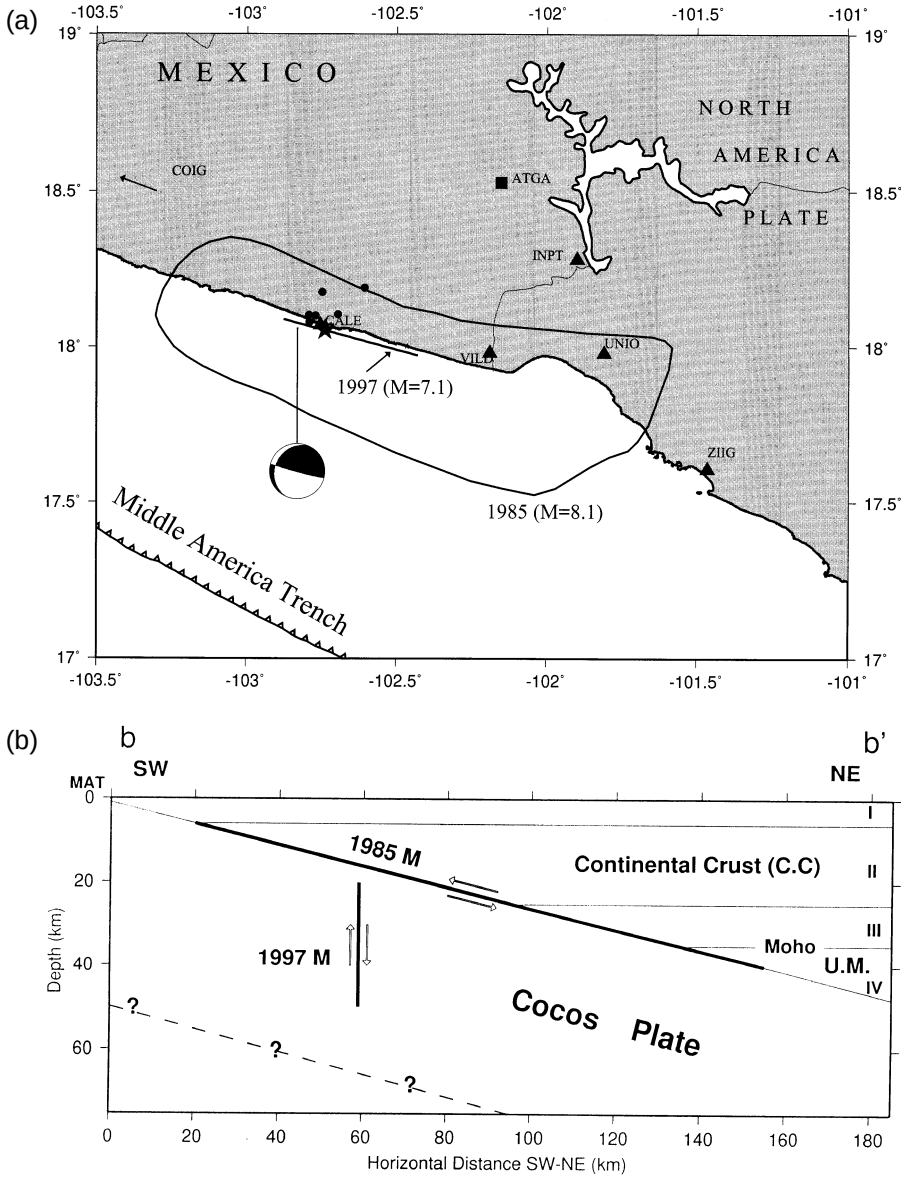


**Figure 1.** (a) Location of the 1997 earthquake (a thick straight line with asterisk near the coast, indicating the horizontal projection of its nearly vertical fault and the epicentre), and the fault plane solution obtained from moment tensor inversion of teleseismic body waves (Santoyo *et al.* 1999). Small solid circles indicate the locations of several aftershocks. A nearly elliptical-shaped curve shows the aftershock zone of the 1985 Michoacan earthquake. Solid triangles indicate strong-motion recording stations in this region. (b) Side-view of the locations of the 1985 thrust event and the 1997 nearly normal faulting earthquake with respect to the subducting Cocos plate and the overlying continental crust and uppermost mantle.

possibility would be the loading of the overriding continental lithosphere temporarily decoupled during the 1985 event from the subducting plate (Singh *et al.* 1985).

Although our previous study (Santoyo *et al.* 1999) revealed the kinematic properties of the fault, including the fault geometry, slip distribution on the fault, average rupture velocity and total source duration of the 1997 event, the fault's dynamic rupture process and the change of stress state have not yet been made clear. In the present study, we develop a 3-D dynamic rupture model for this earthquake in order to clarify its dynamic processes. To accomplish this goal, some of the kinematic fault parameters derived from waveform inversion (Santoyo *et al.* 1999) are used as observational constraints. We derive the rupture pattern and the spatial distribution of dynamic stress drop over the nearly vertical fault. We also discuss the possible effects of stress interaction between the 1985 thrust event and the 1997 earthquake, by comparing the stress-drop distribution with the pattern of coseismic stress change due to the 1985 earthquake.

## KINEMATIC FAULT MODEL

Fig. 1(a) shows the horizontal projection of the 1997 earthquake fault, its fault plane solution, and the locations of near-source strong-motion stations in the Michocan region. The velocity waveforms obtained by integration from the accelerograms recorded at four of these stations (CALE, VILD, INPT

and UNIO) have been used in the kinematic waveform inversion (Santoyo *et al.* 1999). The crust and uppermost mantle structures beneath these stations are slightly different, but in this inversion an average velocity model over the region was used to calculate Green's functions by applying the discrete wavenumber method (Bouchon 1979). The rupture begins at the hypocentre, located at a depth of 35 km and 10 km southeast of the northwestern edge of the fault, and was assumed to propagate circularly at a constant velocity of 2.8 km $s^{-1}$. This velocity gave the best fit between the integrated velocity waveforms and the corresponding synthetic seismograms in the searched range between 2.6 and 3.0 km $s^{-1}$. The velocity source time function was assumed to have a triangular shape with a duration of between 1.0 and 2.0 s, which is the same everywhere on the fault: a duration of 1.2 s was finally adopted. The top of the fault is buried 20 km from the surface, and the fault width and length were taken as 30 km and 50 km, respectively (Fig. 2). For one of the inversions, the fault was divided into a 2 km × 2 km mesh. Fig. 2 shows the slip distribution on the fault, which has been obtained from the inversion with smoothing and positive slip constraints (Santoyo *et al.* 1999). The seismic moment was found to be $3.9 \times 10^{26}$ dyn cm. It is noticed that major slip (> 100 cm) is mostly confined to depths between 25 and 45 km and between 17 and 47 km in the strike direction. Slip larger than 200 cm is concentrated mainly at depths of between 28 and 40 km in the southeastern fault section, and the maximum slip exceeds 300 cm. We derive the dynamic rupture models that follow based on this distribution of kinematic fault slip.

## METHOD OF DYNAMIC RUPTURE MODELLING

The method of dynamic rupture modelling has been described in a number of previous works (Miyatake 1992; Fukuyama & Mikumo 1993; Mikumo & Miyatake 1993, 1995; Beroza & Mikumo 1996; Ide & Takeo 1996, 1997; Mikumo *et al.* 1998), but is again summarized here. The first step is to construct a 3-D dynamic model incorporating a vertical fault in the subducting plate, which is embedded in a horizontally layered half-space. The fault geometry and the rupture starting point have been taken to be the same as those in the above kinematic fault model. We assume that the initial shear stress is applied parallel to the vertical fault, generating pure dip-slip motion on the fault, and that dynamic rupture starts at the point where the initial stress exceeds the prescribed level, and propagates at a constant velocity. We also assume that the shear stress at any point on the fault gradually increases due to the approach of the rupture front, and, for simplicity, drops immediately to the level of dynamic friction at the time of the rupture arrival, which may be regarded as a slip-weakening process with an extremely small slip-weakening distance. The rupture time in the modelling is specified by the kinematic model, and the difference between the assumed initial stress and the dynamic stress is taken as the static stress drop. With these assumptions and given stress drop, the rupture propagation and all displacement components at every point on the fault are calculated successively by solving 3-D wave equations at each time step, with a second-order finite difference scheme under appropriate boundary conditions. At the final time step, we obtain the slip distribution over the fault, called here the final dynamic slip. The boundary conditions imposed are as follows: (a) the ground surface is stress-free; (b) the continuity of all stress and displacement components at each of the layer interfaces; and (c) absorbing boundary conditions (Clayton & Engquist 1977) at the side and bottom boundaries of the model space.

The second step is to evaluate the spatial distribution of dynamic and static stress drops over the fault, from that of the fault slip obtained from waveform inversion in the kinematic model. To do this, we use a non-linear, iterative, least-squares technique. Given approximate estimates of static stress drop on the fault as starting values, we calculate the distribution of

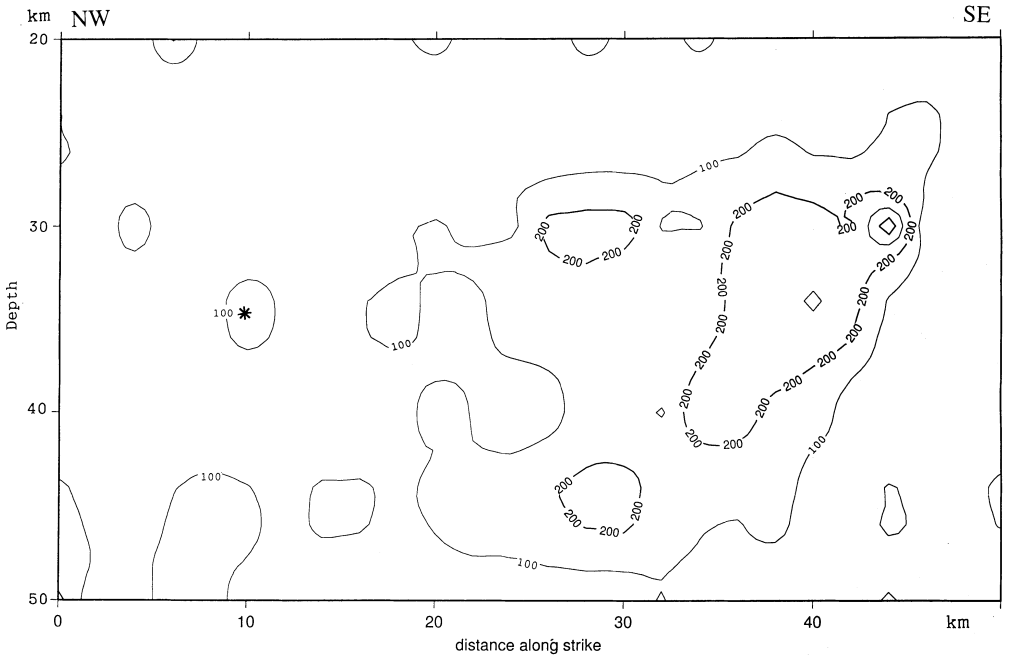


**Figure 2.** Spatial distribution of fault slip (in cm) obtained from kinematic waveform inversion of strong-motion records (Santoyo *et al.* 1999). The asterisk shows the location of the rupture starting point.

dynamic fault slip in the way described above, and compare this with the already-obtained kinematic slip. The ratio between the kinematic and final dynamic slips at each point on the fault is then multiplied, in the next iteration, to the previously estimated stress drop. This procedure is repeated until the rms difference between the kinematic and dynamic slips over the fault can be minimized within a reasonably small value, which gives a best-fitting model. From the final model, we obtain the distribution of dynamic and static stress drops over the fault.

The crust and uppermost structure assumed here is nearly the same as that used in the kinematic model as the average velocity model (Santoyo *et al.* 1999) over the Michoacan region. However, since a more refined model (Valdes & Meyer 1996) in this region shows slightly higher velocities in the subducting Cocos plate, the velocities and densities in the plate are assumed to be higher by 10 per cent than those in the overlying continental crust and uppermost mantle in the same layer. For numerical calculations we take a grid spacing of 2.0 km and a time increment of 0.1 s, in order to be consistent with those in the kinematic model, keeping the stability conditions for wave propagation in the 3-D space. However, these slightly coarse configuration parameters limit the range of wave frequency that can be discussed. The dimension of the model space is 240 km × 137 km × 220 km, and the total number of time steps is taken to be 300 over 30 s.

## DYNAMIC RUPTURE AND STRESS CHANGE

### Model I

Following the method of dynamic rupture modelling described above, we calculate the dynamic slip at each time step at every point on the fault, for a fixed rupture velocity of 2.8 km $s^{-1}$. After repeating the optimization procedure seven times, we obtain the spatial distribution of stress drop with a reasonably small rms difference of 5.8 cm (1.9 per cent of the maximum slip) between the already-obtained kinematic slip and the calculated dynamic slip at the final time step of 30 s. We call this model Model I. Fig. 3 shows the distribution of static stress drop thus obtained over the vertical fault. Comparing this distribution with Fig. 2, we find that quite a large stress drop, higher than 100 bars and even 200 bars in a few localized zones, generated fault slip larger than 200 cm in the southeastern fault section and also at depths of around 30 km and 42 km in the central section. Another feature to be noted is the negative stress-drop zones, mostly near the upper and lower edges of the fault and also in the lower right (southeast) section and some parts of the lower left (northwest) section.

For the next step, we calculate the slip-velocity source time functions at each point on the fault from this dynamic Model I—the results are shown in Fig. 4. To suppress high-frequency numerical noise, we applied a 0.6-s running mean as a high-cut filter and a taper to its later part. The shape of the source time functions is found to vary with the location on the fault, with the duration of the first sharp pulse ranging between 0.5 and 2.0 s. A smaller second bump at some points may be mainly due to the effects of waves reflected back from adjacent high-stress-drop or negative stress-drop segments, but might still be contaminated by numerical noise coming from the coarse grid used here. Nearly flat lines at several points correspond to very low slip.

Next, we calculate the synthetic seismograms by forward modelling, incorporating the slip-velocity source time functions obtained above, in order to compare them with the observed records. To do this, the Green's functions, which were calculated

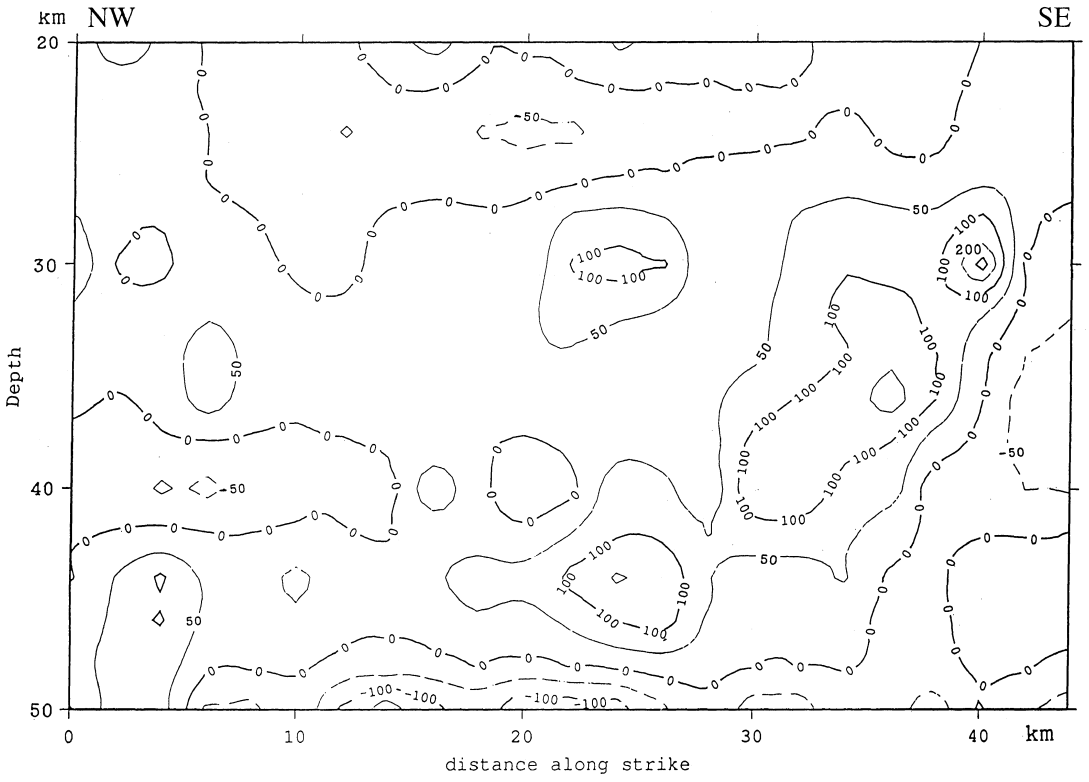


**Figure 3.** Spatial distribution of static stress drop (in bars) (Model I) calculated from the kinematic fault slip in Fig. 2.

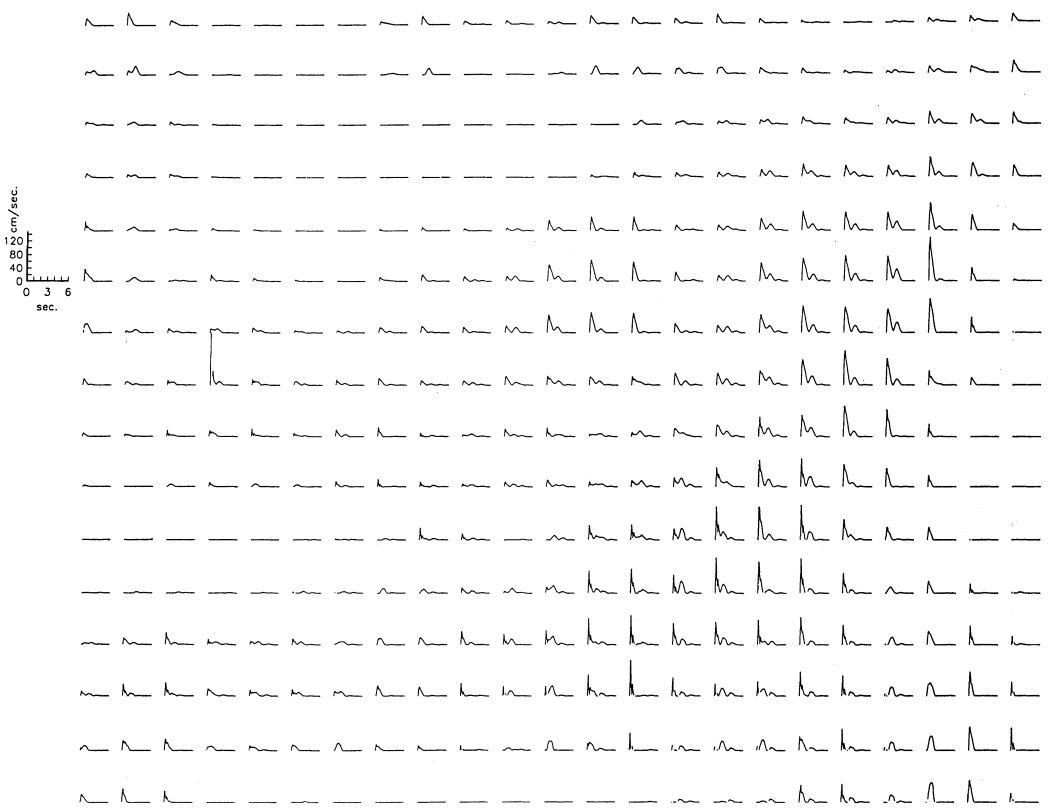


**Figure 4.** Slip-velocity source time functions at selected points on the fault, calculated from Model I. All the initial times of these time functions are shifted to zero from the arrival time of rupture at these points. Locations are arranged from the top to the bottom and from NW (left) to SE (right) on the vertical fault.

when obtaining the kinematic model, are convolved with the above dynamically generated source time functions, and are integrated over the fault plane. In view of the grid spacing used in the numerical calculations, the minimum wavelength (8 km) needed for wave propagation without grid dispersion means that the reliable upper frequency limit is less than 0.5 Hz. Accordingly, the calculated synthetic seismograms and the observed strong-motion velocity records are low-pass filtered with a cut-off frequency of 0.5 Hz; the results are shown in Fig. 5. The comparison gives quite a good fit between the synthetic and observed waveforms, except for the EW component at the INPT and UNIO stations and the vertical component at CALE. The rms difference between the recorded and synthetic waveforms for each component is given in Table 1.

## Model II

In order to improve the above model, we perform another waveform inversion using the low-pass filtered velocity records as the observed data, incorporating the dynamically generated slip-velocity time functions shown in Fig. 4, instead of using an *a priori* assumed source time function. In this inversion, again with smoothing and positive slip constraints, only slip is allowed to vary, with a fixed rupture velocity of 2.8 km $s^{-1}$. Fig. 6 gives the spatial distribution of fault slip derived from this dynamically consistent inversion. The pattern of slip distribution is quite different from that in Fig. 2, and appears to be more confined to the lower half of the vertical fault, and also the slip amplitude in some sections is larger than in the original kinematic model. This concentration of slip patterns has been

**Table 1.** The degree of misfit between the recorded and synthetic waveforms, given by the rms difference ($\sigma/R_m$) between the two types of waveforms.

| Comp. | MODEL I | | | | MODEL II | | | |
|---|---|---|---|---|---|---|---|---|
| | CALE | VILE | INPT | UNIO | CALE | VILE | INPT | UNIO |
| V | 0.336 | 0.199 | 0.179 | 0.201 | 0.333 | 0.173 | 0.097 | 0.122 |
| EW | 0.199 | 0.191 | 0.278 | 0.213 | 0.135 | 0.137 | 0.303 | 0.262 |
| NS | 0.198 | 0.108 | 0.241 | 0.166 | 0.084 | 0.074 | 0.272 | 0.165 |

$\sigma = \{\Sigma_{j=1}^{N} [R(t_j) - cS(t_j)]^2/N\}^{1/2}$; $c = R_m/S_m$ (a normalization constant) where $R$ and $S$ denote the recorded and synthetic waveforms

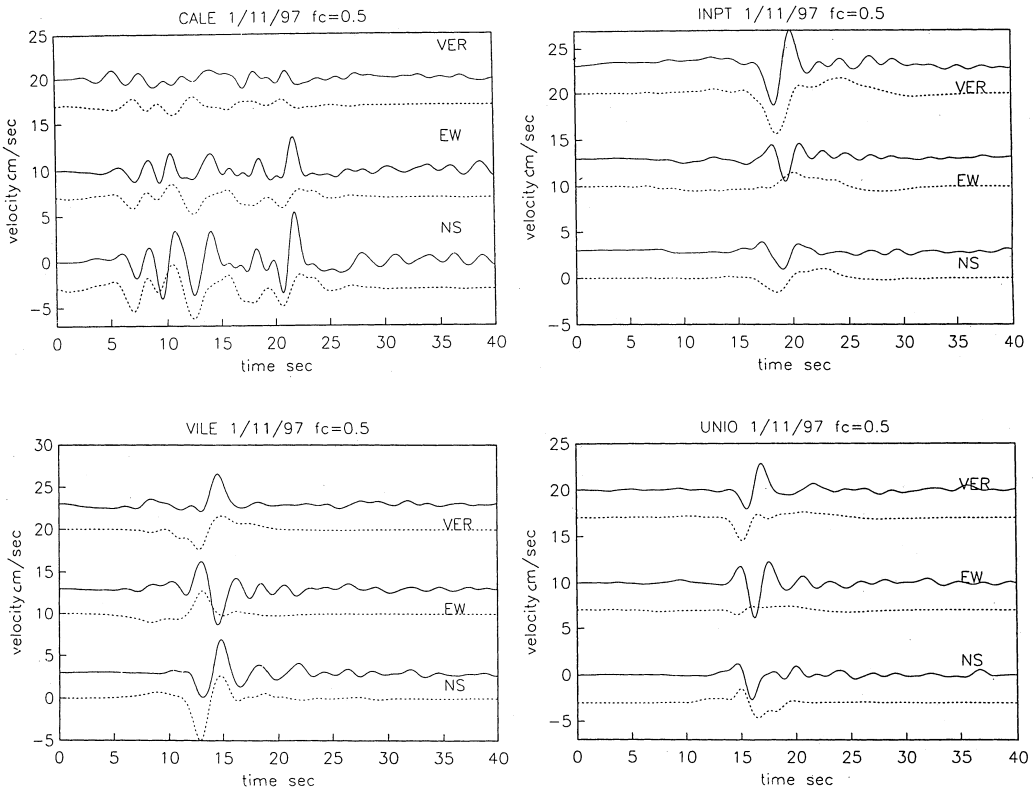


**Figure 5.** Low-pass filtered (<0.5 Hz) strong-motion velocity records (continuous lines), and the corresponding synthetic seismograms (dotted lines) calculated from Model I by forward modelling with the dynamically generated source time functions.

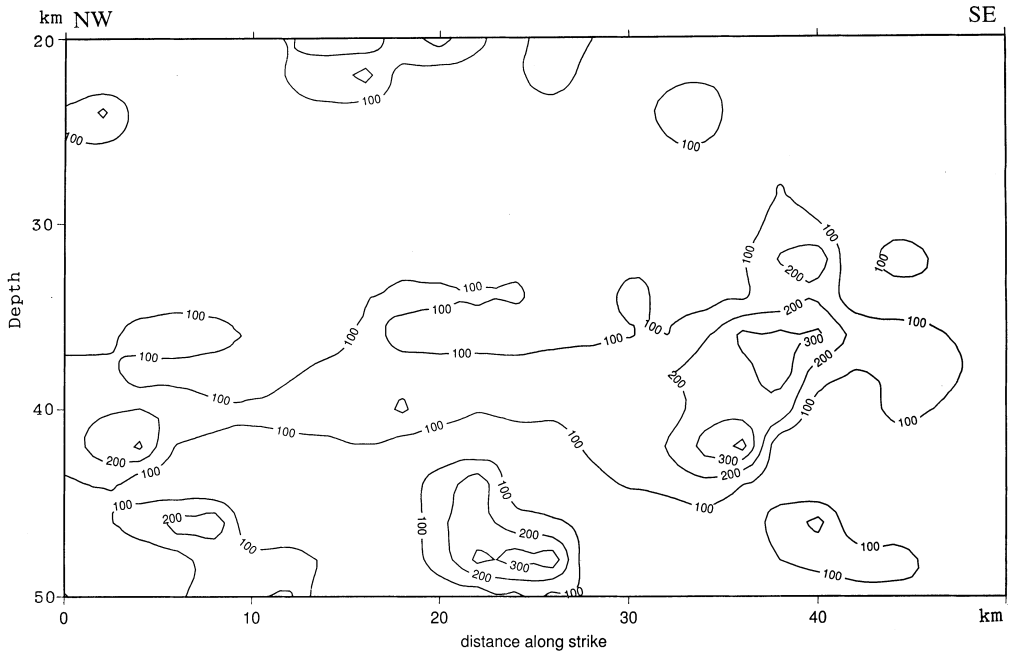


**Figure 6.** Spatial distribution of fault slip (in cm) derived from waveform inversion of the low-pass filtered strong-motion records, incorporating the dynamically generated slip-velocity source time functions.

noted by Beroza & Mikumo (1996), who also performed a dynamically consistent waveform inversion. The zone of major slip, with the maximum slip exceeding 300 cm, is still located at depths between 30 and 45 km, and between 35 and 40 km in the strike direction. Another high-slip zone, with slip larger than 200 cm, appears in the deepest middle section, and the mid-depth high-slip zone extends to the northwest fault section.

We calculate static stress drop from the above slip distribution given in Fig. 6 through the optimization procedure described above, again with a fixed rupture velocity of 2.8 km $s^{-1}$. The rms difference between the slip given in Fig. 6 and the final dynamic slip is now 4.4 cm (1.4 per cent of the maximum slip), which is slightly better than that in Model I. Fig. 7 shows the distribution of static stress drop in this improved dynamic model, which we call Model II. Again, the zones of high stress drop (> 100 bars) are located below 30 km and are mostly confined to certain areas: one is in the southeastern section at depths between 30 and 43 km, and 32 and 42 km in the strike direction, where the maximum stress drop reaches 280 bars; the second, with stress drop exceeding 200 bars, is in the middle section below 45 km; and the other three, having stress drops between 100 and 150 bars, are located in the strike direction between 14 and 20 km, between 5 and 10 km and between 0 and 7 km. These patch-like high-stress-drop zones may be regarded as asperities.

The synthetic seismograms calculated from the above inversion and the corresponding low-pass filtered records are shown in Fig. 8. The fit appears be slightly improved. The rms differences between the recorded and synthetic waveforms are given in Table 1, along with those for Model I. There still remains, however, a slight phase shift in the EW and NS components at INPT. The EW component at UNIO shows a nearly reverse sense or a considerable phase delay to the observed record. This discrepancy, which was also pointed out in the above kinematic inversion, would not be reconciled by further inversions. The discrepancy might be attributable to possible lateral variations in the upper crustal structure between the two stations (Santoyo *et al.* 1999), which are not included in the theoretical Green's functions.

## DISCUSSION

### Comparison between Model I and Model II

The dynamically consistent waveform inversion of the low-pass filtered velocity records provided the slip distribution (Fig. 6) and stress-drop distribution (Fig. 7) for Model II, while Figs 2 and 3 show the corresponding slip and stress-drop distributions for Model I, respectively. As mentioned above, Model II gives a slightly smaller rms difference between the inverted slip and the final dynamic slip than Model I. Table 1 gives the rms differences between the recorded and synthetic waveforms for three components at each of the four stations in Models I and II. It can be seen from the Table that the fit between the two types of waveforms in Model II has been improved to some extent, as compared with that in Model I, except for the EW and NS components at INPT and the EW component at UNIO. The fairly large rms values for these components are due to the reverse sense and the phase mismatch, as in Model I. From these comparisons, we can regard Model II as the preferred model in this study, although Model I still cannot be totally ruled out.

### Heterogeneous stress-drop distribution

The two models reveal a highly heterogeneous distribution of static stress drop and fault slip over the nearly vertical fault. Zones of high stress drop are mainly concentrated in the southeastern fault section, at depths between 30 and 45 km. Several other patch-like zones of relatively high stress drop can be identified, but a few isolated patches might be spurious,

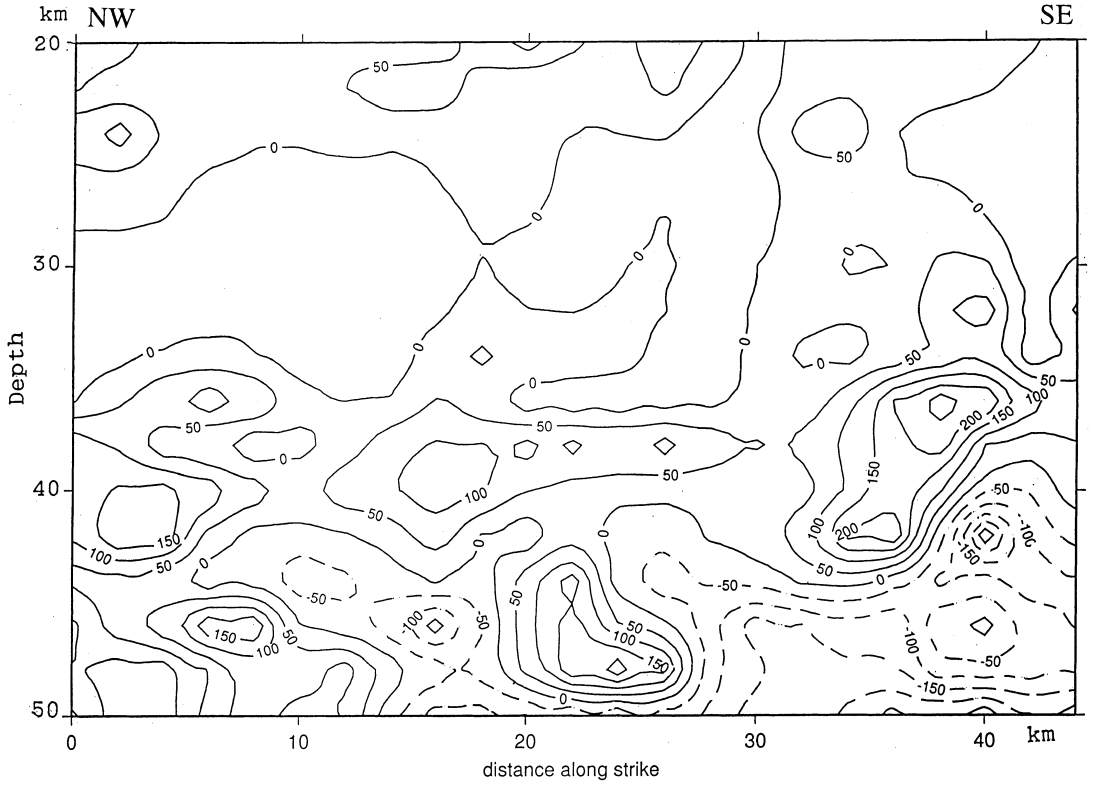


**Figure 7.** Spatial distribution of static stress drop (in bars) (Model II) calculated from the fault slip (Fig. 6).

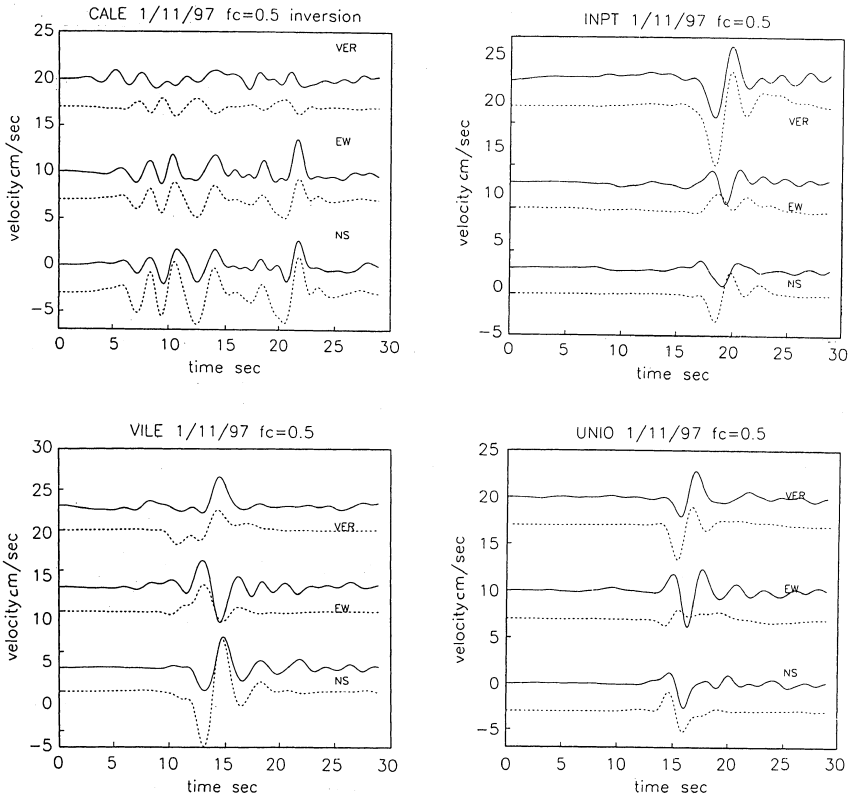


**Figure 8.** Low-pass filtered (<0.5 Hz) strong-motion velocity records (continuous lines), and the corresponding synthetic seismograms (dotted lines) calculated from Model II by waveform inversion of the filtered records, incorporating the dynamically generated source time functions. (The amplitude of the NS record at CALE has been reduced for convenience by half in this plot).

resulting from numerical noise included in the inversion. Zones of negative stress drop are distributed in between the zones of high stress drop and near the upper and lower edges of the fault. These negative drops (stress increases) are required to account for very low slip, and also partly to compensate the high stress drops (stress decreases). However, the negative values near the fault edges may be due to the edge effect. Some uncertainties and less well-resolved slip on some subfaults that might be included in the inversions, partly because of the somewhat coarse grid used and possible uncertainties in the velocity model, would affect the estimate of dynamic and static stress drop almost linearly. For these reasons, the absolute values of stress drop could involve uncertainties probably much larger than 10 per cent, although it is difficult to give an exact estimate of these uncertainties because of the non-linear properties of the problem. Nevertheless, the maximum stress drop in a localized zone in the southeastern fault section exceeds 280 bars. This is significantly larger than the maximum drop of 130 bars during the 1985 thrust earthquake (Mikumo *et al.* 1998). The difference suggests that the stress resistance to shear fracture in the subducting plate may be considerably higher than that on the upper interface of the plate, although the direction of the applied shear stress is different.

### Short slip duration

It is found that the slip duration in the velocity source time functions calculated from the dynamic model ranges between 0.5 and 2.0 s, although some of the source time functions are perturbed by subsequent small bumps. The duration is quite short compared with a simple estimate for the time needed for the rupture to travel across half of the shorter dimension of the fault (Day 1982). The short slip duration in the fault can be entirely attributed to the short scalelength of stress-drop heterogeneities, including negative stress-drop zones, making it unnecessary to introduce any specific self-healing mechanism (e.g. Heaton 1990), as has been demonstrated and discussed in some detail in a previous work on the 1984 Morgan Hill, California, earthquake (Beroza & Mikumo 1996). A similar conclusion was reached in the cases of the 1995 Kobe, Japan earthquake (Ide & Takeo 1997), and the 1992 Landers and 1994 Northridge, California, earthquakes (Day *et al.* 1998). A possible interpretation is that negative stress-drop zones in these cases provide geometrical constraints, which preclude further extension of slip and thus will generate healing pulses. Day *et al.* (1998) found further evidence favouring this model, in that a pronounced recovery of shear stress after the passage of a rupture front, which is considered inherent to the self-healing hypothesis, cannot be detected from their inversion analysis. However, the limited spatial and time resolutions in the present kinematic and dynamic models mean that the possible existence of self-healing, frictional fault behaviour cannot be totally ruled out. It is to be emphasized that the present dynamic model with 'velocity-independent' friction and an extremely small slip-weakening distance provided this type of short slip duration, and has been proved to be consistent with the strong-motion data obtained.

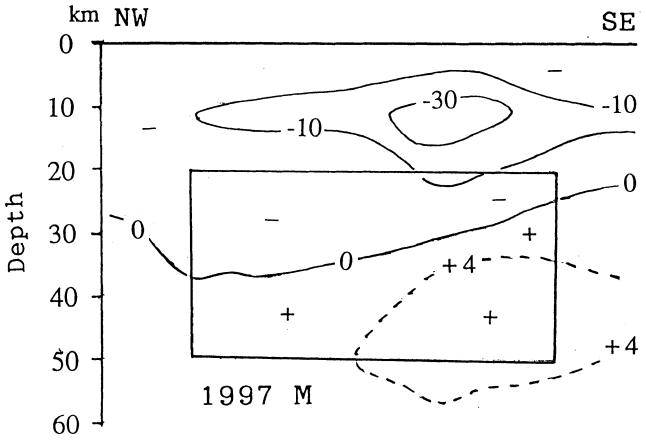


**Figure 9.** Calculated coseismic changes in the shear stress (in bars) on the 1997 vertical fault due to the 1985 thrust event.

### Possible stress transfer from the 1985 thrust earthquake

Mikumo *et al.* (1999) estimated the coseismic stress change in the subducting Cocos plate due to the 1985 thrust event. Fig. 9 shows the coseismic change in shear stress along the vertical fault plane of the 1997 earthquake, with the fault zone enclosed by a rectangle. It is clear that the shear stress after the 1985 event dropped in the upper section of the 1997 fault to its minimum below a high-stress-drop zone of the 1985 event. In the lower fault section, on the other hand, the shear stress increased by up to 5 bars. The zone of stress increase appears to be separated from that of stress decrease by an oblique lobe traversing nearly the mid-depth of the fault. Comparing this pattern with the slip (Fig. 6) and stress-drop (Fig. 7) distributions from the 1997 earthquake, we notice that large slip and high stress drop took place in the zone of previous stress increase in the lower fault section, while only small slip and negative stress drop occurred in the zone of previous stress decrease in the upper part. The pattern of coseismic stress change (Fig. 9) due to the 1985 thrust event and that of stress drop (Fig. 7) during the 1997 earthquake have been derived from completely different observations. We are inclined to believe that their similar patterns are not just a coincidence but indicate a physical interaction between them. We may conclude that the 1997 near-vertical, normal faulting earthquake occurred under some stress transfer from the 1985 large thrust event to the subducting plate just beneath it, and possibly with postseismic stress increase up to the time of the 1997 event.

## CONCLUSIONS

We have investigated the dynamic rupture and resultant stress change in the 1997 nearly vertical, normal faulting earthquake that occurred in the subducting Cocos plate just beneath the ruptured fault zone of the great 1985 Michoacan earthquake, on the basis of near-source strong-motion observations together with a 3-D dynamic model. The main results are summarized below.

(1) A highly heterogeneous stress-drop distribution has been revealed by dynamically consistent waveform inversions. High-stress-drop zones are mainly confined to the deeper part of the southeastern side of the fault, and are surrounded by negative stress-drop zones. The maximum stress drop reaches 280 bars (28 MPa). This is significantly larger than that experienced during the 1985 thrust earthquake that occurred on the upper interface of the subducting slab, suggesting the existence of higher stress within the slab.

(2) The dynamically generated slip-velocity source time functions have a short slip duration, ranging between 0.5 and 2.0 s. This short duration can be attributed to the short scale-length of stress-drop heterogeneities, particularly including negative stress-drop zones. The synthetic waveforms derived from the dynamic model with these source time functions and heterogeneous stress drop are generally consistent with the strong-motion records in the frequency range lower than 0.5 Hz.

(3) The stress-drop distribution on the vertical fault of the present 1997 earthquake appears to be consistent with the pattern of coseismic stress changes caused over the fault by the 1985 thrust earthquake. This consistency suggests that the stress transfer from the 1985 event down to the interior of the subducting plate could be one possible source that enhanced the chance of occurrence of the 1997 earthquake.

## ACKNOWLEDGMENTS

We are grateful to the critical reviews and constructive comments given by Raul Madariaga and Steve Day, which greatly improved our original manuscript. We also thank Masayuki Kikuchi for providing us with early information on the moment tensor inversion of the 1997 earthquake.

## REFERENCES

Beroza, G. & Mikumo, T., 1996. Short slip duration in dynamic rupture in the presence of heterogeneous fault properties, *J. geophys. Res.,* **101,** 22 449–22 460.

Bouchon, M., 1979. Discrete wave number representation of elastic wave fields in three-space dimensions, *J. geophys. Res.,* **84,** 3609–3614.

Clayton, R. & Engquist, B., 1977. Absorbing boundary conditions for acoustic and elastic wave equations, *Bull. seism. Soc. Am.,* **67,** 1529–1540.

Cocco, M., Pacheco, J., Singh, S.K. & Courboulex, F., 1997. The Zihuatanejo, Mexico, earthquake of 1994 December 10 (M = 6.6): source characteristics and tectonic implications, *Geophys. J. Int.,* **131,** 135–145.

Day, S.M., 1982. Three-dimensional finite difference simulation of fault dynamics: Rectangular faults with fixed rupture velocity, *Bull. seism. Soc. Am.,* **72,** 705–727.

Day, S.M., Yu, G. & Wald, D.J., 1998. Dynamic stress change during earthquake rupture, *Bull. seism. Soc. Am.,* **88,** 512–522.

Fukuyama, E. & Mikumo, T., 1993. Dynamic rupture analysis: inversion for the source process of the 1990 Izu Oshima, Japan earthquake (M6.5), *J. geophys. Res.,* **98,** 6529–6542.

Heaton, T.H., 1990. Evidence for implications of self-healing pulses of slip in earthquake rupture, *Phys. Earth planet. Inter.,* **64,** 1–29.

Ide, S. & Takeo, M., 1996. The dynamic rupture process of the 1993 Kushiro-oki earthquake, *J. geophys. Res.,* **101,** 5661–5675.

Ide, S. & Takeo, M., 1997. Determination of constitutive relations of fault slip based on seismic wave analysis, *J. geophys. Res.,* **102,** 23 379–23 391.

Mikumo, T. & Miyatake, T., 1993. Dynamic rupture processes on a dipping fault, and estimates of stress drop and strength excess from the results of waveform inversion, *Geophys. J. Int.,* **112,** 481–496.

Mikumo, T. & Miyatake, T., 1995. Heterogeneous distribution of dynamic stress drop and relative fault strength recovered from the results of waveform inversion: the 1984 Morgan Hill, California, earthquake, *Bull. seism. Soc. Am.,* **85,** 178–193.

Mikumo, T., Miyatake, T. & Santoyo, M.A., 1998. Dynamic rupture of asperities and stress change during a sequence of large interplate earthquakes in the Mexican subduction zone, *Bull. seism. Soc. Am.,* **88,** 686–702.

Mikumo, T., Singh, S.K. & Santoyo, M.A., 1999. A possible stress interaction between large thrust and normal faulting earthquakes in the Mexican subduction zone, *Bull. seism. Soc. Am.,* **89,** in press.

Miyatake, T., 1992. Reconstruction of dynamic rupture process of an earthquake with constraints of kinematic parameters, *Geophys. Res. Lett.,* **19,** 349–352.

Quintanar, L., Yamamoto, J. & Jimenez, Z., 1999. Source mechanism of two intermediate depth focus earthquakes in Guerrero, Mexico, *Bull. seism. Soc. Am.,* **89,** 845–853.

Santoyo, M.A., Singh, S.K. & Mikumo, T., 1999. Source characteristics of the 11 January, 1997 Michoacan, Mexico earthquake (Mw = 7.1), *Bull. seism. Soc. Am.,* to be submitted.

Singh, S.K. & Wyss, M., 1976. Source parameters of the Orizaba earthquake of August 28, 1973, *Geof. Int.,* **16,** 165–194.

Singh, S.K., Suarez, G. & Dominguez, T., 1985. The Oaxaca, Mexico, earthquake of 1931: Lithospheric normal faulting in the subducted Cocos plate, *Nature,* **317,** 56–58.

Singh, S.K., Ordaz, M. & Perez-Rocha, L.E., 1996. The great Mexican earthquake of 1858: Expected ground motions in Mexico City from a similar future event, *Bull. seism. Soc. Am.,* **86,** 1655–1666.

Valdes, C. & Meyer, R.P., 1996. Seismic structure between the Pacific coast and Mexico City from the Petatlan earthquake ($M_S = 7.6$) aftershocks, *Geof. Int.,* **35,** 377–401.

Yamamoto, J., Jimenez, Z. & Mota, R., 1984. El temblor de Huajuapan de Leon, Oaxaca, Mexico, del 24 de octubre de 1980, *Geof. Int.,* **23,** 83–110.